p-$GaInP_2$/TiO_2 exhibit oscillations similar to that for p-$GaInP_2$/Pt, meaning that the surface field increases substantially when the TiO_2 thickness increases from 0.5 to 35 nm. The formation and decay time constant of ΔF for these samples are extracted from the corresponding TPR kinetics (fig. S9B). Best-fit parameters are tabulated in table S1. Thicker TiO_2 layers exhibit slightly faster field formation but slower decay, which is likely due to the larger built-in field that drives carriers apart and separates them at a greater distance, both of which lead to slower recombination. We find that the kinetics are effectively unperturbed once a sufficient amorphous TiO_2 thickness has been reached, suggesting that thicker layers would not drastically influence the photoconversion performance from a charge dynamics perspective. A thick TiO_2 layer may still be necessary for other reasons (such as elimination of pinholes) that affect stabilization against photocorrosion, as has been found for 140-nm-thick amorphous TiO_2 layers on Si, GaAs, and GaP photoanodes (*2*).

Our results uncover key beneficial roles of amorphous TiO_2 in the energy-conversion process that have come under intense investigation after several recent reports of TiO_2-stablized photoelectrodes (*2*, *29*, *30*). The TPR technique developed here furthermore introduces a general method to understand charge transfer at semiconductor junctions.

REFERENCES AND NOTES

1. A. Fujishima, K. Honda, *Nature* **238**, 37–38 (1972).
2. S. Hu *et al.*, *Science* **344**, 1005–1009 (2014).
3. O. Khaselev, J. A. Turner, *Science* **280**, 425–427 (1998).
4. M. Grätzel, *Nature* **414**, 338–344 (2001).
5. N. S. Lewis, D. G. Nocera, *Proc. Natl. Acad. Sci. U.S.A.* **103**, 15729–15735 (2006).
6. M. C. Beard, G. M. Turner, C. A. Schmuttenmaer, *J. Phys. Chem. B* **106**, 7146–7159 (2002).
7. R. Ulbricht, E. Hendry, J. Shan, T. F. Heinz, M. Bonn, *Rev. Mod. Phys.* **83**, 543–586 (2011).
8. J. Shah, *Ultrafast Spectroscopy of Semiconductors and Semiconductor Nanostructures* (Springer, Berlin and Heidelberg, ed. 2, 1999).
9. Y. Yang, T. Lian, *Coord. Chem. Rev.* **263-264**, 229–238 (2014).
10. K. Tvrdy, P. A. Frantsuzov, P. V. Kamat, *Proc. Natl. Acad. Sci. U.S.A.* **108**, 29–34 (2011).
11. K. E. Knowles, M. D. Peterson, M. R. McPhail, E. A. Weiss, *J. Phys. Chem. C* **117**, 10229–10243 (2013).
12. V. I. Klimov, *Annu. Rev. Phys. Chem.* **58**, 635–673 (2007).
13. W. A. Tisdale *et al.*, *Science* **328**, 1543–1547 (2010).
14. Z. Chen *et al.*, *J. Mater. Res.* **25**, 3–16 (2010).
15. B. R. Bennett, R. A. Soref, J. A. del Alamo, *IEEE J. Quantum Electron.* **26**, 113–122 (1990).
16. D. E. Aspnes, *Phys. Rev. Lett.* **28**, 168–171 (1972).
17. S. Marcinkevičius *et al.*, *AIP Adv* **2**, 042148 (2012).
18. P. Emanuelsson *et al.*, *Appl. Phys. Lett.* **64**, 2849–2851 (1994).
19. K. L. Vodopyanov, H. Graener, C. C. Phillips, T. J. Tate, *Phys. Rev. B* **46**, 13194–13200 (1992).
20. A. J. Sabbah, D. M. Riffe, *J. Appl. Phys.* **88**, 6954–6956 (2000).
21. Y. Yang *et al.*, *Nat. Commun.* **6**, 7961 (2015).
22. H. Shen, M. Dutta, *J. Appl. Phys.* **78**, 2151–2176 (1995).
23. T. Kippenberg *et al.*, *Phys. Rev. B* **60**, 4446–4449 (1999).
24. F. H. Pollak, *Surf. Interface Anal.* **31**, 938–953 (2001).
25. H. Shen, F. H. Pollak, *Phys. Rev. B* **42**, 7097–7102 (1990).
26. T. Kita *et al.*, *J. Appl. Phys.* **94**, 6487–6490 (2003).
27. Y. S. Huang *et al.*, *Appl. Phys. Lett.* **73**, 214–216 (1998).
28. F. J. Schultes *et al.*, *Appl. Phys. Lett.* **103**, 242106 (2013).
29. B. Seger *et al.*, *J. Am. Chem. Soc.* **135**, 1057–1064 (2013).
30. B. Seger *et al.*, *RSC Adv.* **3**, 25902–25907 (2013).

ACKNOWLEDGMENTS

This work was supported by the Division of Chemical Sciences, Geosciences and Biosciences, Office of Basic Energy Sciences of the U.S. Department of Energy, through the Solar Photochemistry Program under contract no. DE-AC36-08GO28308 to the National Renewable Energy Laboratory. J.L.Y. acknowledges NSF Graduate Research Fellowship Grant no. DGE 1144083. The U.S. government retains—and the publisher, by accepting the article for publication, acknowledges that the U.S. government retains—a nonexclusive, paid-up, irrevocable, worldwide license to publish or reproduce the published form of this work, or allow others to do so, for U.S. government purposes.

SUPPLEMENTARY MATERIALS

www.sciencemag.org/content/350/6264/1061/suppl/DC1
Materials and Methods
Figs. S1 to S9
Tables S1 to S4
References (*31*, *32*)

31 August 2015; accepted 19 October 2015
10.1126/science.aad3459

NANOMATERIALS

Near-unity photoluminescence quantum yield in MoS_2

Matin Amani,[1,2]* Der-Hsien Lien,[1,2,3,4]* Daisuke Kiriya,[1,2]* Jun Xiao,[5,2] Angelica Azcatl,[6] Jiyoung Noh,[6] Surabhi R. Madhvapathy,[1,2] Rafik Addou,[6] Santosh KC,[6] Madan Dubey,[7] Kyeongjae Cho,[6] Robert M. Wallace,[6] Si-Chen Lee,[4] Jr-Hau He,[3] Joel W. Ager III,[2] Xiang Zhang,[5,2,8] Eli Yablonovitch,[1,2] Ali Javey[1,2]†

Two-dimensional (2D) transition metal dichalcogenides have emerged as a promising material system for optoelectronic applications, but their primary figure of merit, the room-temperature photoluminescence quantum yield (QY), is extremely low. The prototypical 2D material molybdenum disulfide (MoS_2) is reported to have a maximum QY of 0.6%, which indicates a considerable defect density. Here we report on an air-stable, solution-based chemical treatment by an organic superacid, which uniformly enhances the photoluminescence and minority carrier lifetime of MoS_2 monolayers by more than two orders of magnitude. The treatment eliminates defect-mediated nonradiative recombination, thus resulting in a final QY of more than 95%, with a longest-observed lifetime of 10.8 0.6 nanoseconds. Our ability to obtain optoelectronic monolayers with near-perfect properties opens the door for the development of highly efficient light-emitting diodes, lasers, and solar cells based on 2D materials.

Monolayer transition metal dichalcogenides (TMDCs) have properties that make them highly suitable for optoelectronics (*1*, *2*), including the ability to form van der Waals heterostructures without the need for lattice matching (*3*, *4*), circular dichroism arising from the direct band gap occurring at the K and K′ points of the Brillouin zone (*5*), and widely tunable band structure through the application of external forces such as electric field and strain (*6*). Unlike III-V semiconductors, the optical properties of TMDCs are dominated by excitons with strong binding energies (on the order of 300 meV) (*7*–*9*) and large radii (~1.6 nm) (*10*). However, TMDCs have exhibited poor luminescence quantum yield (QY)—that is, the number of photons the material radiates is much lower than the number of generated electron-hole pairs. QY values ranging from 0.01 to 6% have been reported, indicating a high density of defect states and mediocre electronic quality (*11*–*13*). The origin of the low quantum yield observed in these materials is attributed to defect-mediated nonradiative recombination and biexcitonic recombination at higher excitation powers (*11*, *13*).

Two-dimensional (2D) monolayers are amenable to surface passivation by chemical treatments. We studied a wide range of chemical treatments and describe here an air-stable, solution-based process using an organic superacid that removes the contribution of defect-mediated nonradiative recombination acting on electronically active defect sites by uniformly passivating them, repairing them, or both. With the use of this process, the photoluminescence (PL) in MoS_2 monolayers

[1]Electrical Engineering and Computer Sciences, University of California, Berkeley, Berkeley, CA 94720, USA. [2]Materials Sciences Division, Lawrence Berkeley National Laboratory, Berkeley, CA 94720, USA. [3]Computer, Electrical and Mathematical Sciences and Engineering Division, King Abdullah University of Science and Technology (KAUST), Thuwal 23955-6900, Saudi Arabia. [4]Department of Electrical Engineering, Institute of Electronics Engineering, National Taiwan University, Taipei 10617, Taiwan, Republic of China. [5]National Science Foundation Nanoscale Science and Engineering Center, University of California, Berkeley, Berkeley, CA 94720, USA. [6]Department of Materials Science and Engineering, University of Texas, Dallas, Richardson, TX 75080, USA. [7]Sensors and Electron Devices Directorate, U.S. Army Research Laboratory, Adelphi, MD 20723, USA. [8]Department of Physics, King Abdulaziz University, Jeddah 21589, Saudi Arabia.
*These authors contributed equally to this work. **†Corresponding author. E-mail: ajavey@eecs.berkeley.edu**

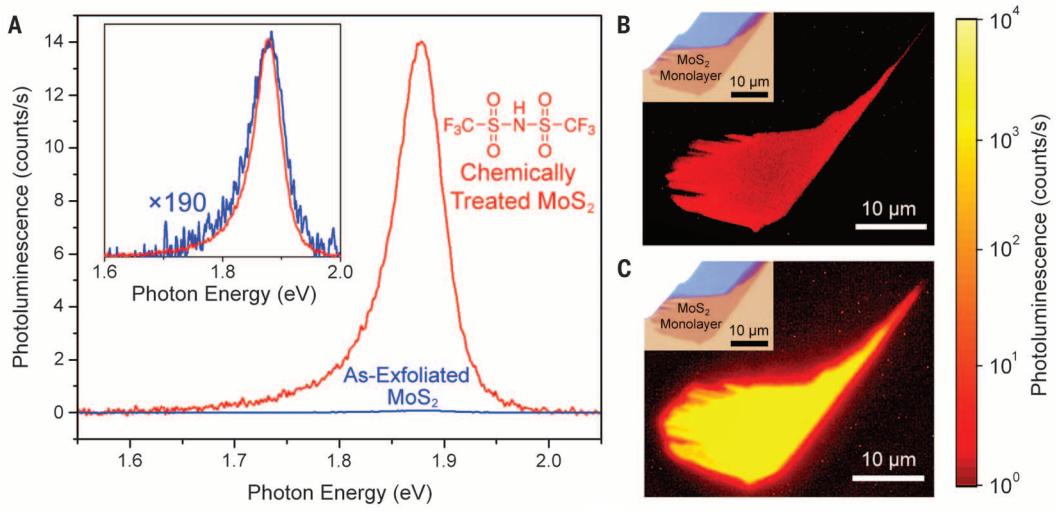

Fig. 1. Enhancement of PL by chemical treatment. (**A**) PL spectrum for both the as-exfoliated and TFSI-treated MoS_2 monolayers measured at an incident power of 1×10^{-2} W cm^{-2}. The inset shows normalized spectra. (**B** and **C**) PL images of a MoS_2 monolayer before (B) and after treatment (C). Insets show optical micrographs.

increased by more than two orders of magnitude, resulting in a QY > 95% and a characteristic lifetime of 10.8 ± 0.6 ns at low excitation densities.

In this study, we treated MoS_2 monolayers with a nonoxidizing organic superacid: bis(trifluoromethane) sulfonimide (TFSI). Superacids are strong protonating agents and have a Hammett acidity function (H_0) that is lower than that of pure sulfuric acid. [Details of the sample preparation and treatment procedure are discussed in the supplementary materials and methods (*14*).] The PL spectra of a MoS_2 monolayer measured before and after TFSI treatment (Fig. 1A) show a 190-fold increase in the PL peak intensity, with no change in the overall spectral shape. The magnitude of the enhancement depended strongly on the quality of the original as-exfoliated monolayer (*14*). (The term "as-exfoliated" indicates that the MoS_2 flakes were not processed after exfoliation.) PL images of a monolayer (Fig. 1, B and C, and fig. S4) (*14*), taken before and after treatment at the same illumination conditions, show that the enhancement from the superacid treatment is spatially uniform.

Calibrated steady-state PL measurements (*14*) showed that the spectral shape of the emission remained unchanged over a pump intensity dynamic range spanning six orders of magnitude (10^{-4} to 10^{2} W cm^{-2}) (fig. S2) (*14*). From the pump-power dependence of the calibrated luminescence intensity (Fig. 2A), we extracted the QY (Fig. 2B). As-exfoliated samples exhibited low QY, with a peak efficiency of 1% measured at 10^{-2} W cm^{-2}. The absolute efficiency (*12*, *13*) and observed power law (*13*) are consistent with previous reports for exfoliated MoS_2. After TFSI treatment, the QY reached a plateau at a low pump intensity (<10^{-2} W cm^{-2}), with a maximum value greater than 95%. The near-unity QY suggests that, within this range of incident power, there was negligible nonradiative recombination occurring in the sample. Although pure radiative recombination is commonly observed for fluorescent molecules that inherently have no dangling bonds, only a few semiconductors, such as GaAs double heterostructures (*15*) and surface-passivated quantum dots (*16*), show this behavior at room temperature.

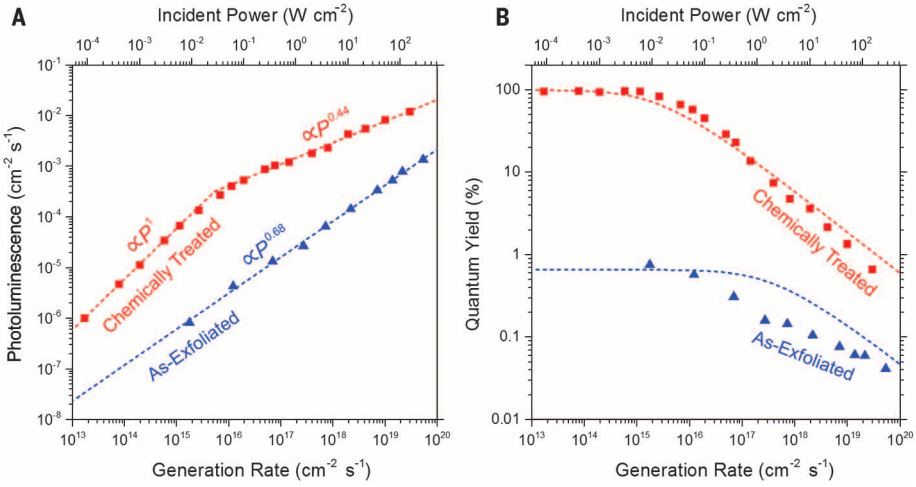

Fig. 2. Steady-state luminescence. (**A**) Pump-power dependence of the integrated PL for as-exfoliated and treated MoS_2. Dashed lines show power law fits for the three dominant recombination regimes. (**B**) Pump-power dependence of the QY for as-exfoliated and treated MoS_2. Dashed lines show the recombination model.

At high pump power, we observed a sharp drop-off in the QY, possibly caused by nonradiative biexcitonic recombination. We consider several models to explain the carrier density–dependent recombination mechanisms in MoS_2 before and after TFSI treatment. Here, n and p are the 2D electron and hole concentrations, respectively. At high-level injection, the dopant concentration is much less than the number of optically generated carriers, allowing $n = p$. The traditional interpretation without excitons (*17*) invokes a total recombination, R, as $R = An + Bn^2 + Cn^3$, where A is the Shockley-Read-Hall (SRH) recombination rate, B is the radiative recombination rate, and C is the Auger recombination rate. The QY is given as the radiative recombination rate over the total recombination. Auger processes dominate at high carrier concentrations, whereas SRH recombination dominates at low carrier concentrations. In the SRH regime (i.e., low pump power), QY increases with pump intensity. This behavior, however, was not observed in previous MoS_2 studies (*12*, *13*) or in this work.

The standard model poorly describes our QY data (fig. S10) (*14*), which are strongly influenced by bound excitons (*9*). As a result, the radiative rate is proportional to the total exciton population, $\langle N \rangle$ (*18*). At high exciton densities, nonradiative biexcitonic recombination can dominate, leading to a recombination rate proportional to $\langle N \rangle^2$ (*18*). Previous reports also suggest that the luminescence in as-exfoliated samples is limited by nonradiative defect-mediated processes (*19*, *20*), resulting in low QY. Although the precise nature of the defect-mediated nonradiative recombination is unclear, a simple analytical model can be developed to describe our experimental results. The total excitation rate, R, in MoS_2 is balanced by recombination

$$R = B_{nr}n^2 + B_r n^2 \quad (1)$$

where B_{nr} is the nonradiative defect-mediated recombination rate and B_r is the formation rate of excitons. The generated excitons can then either

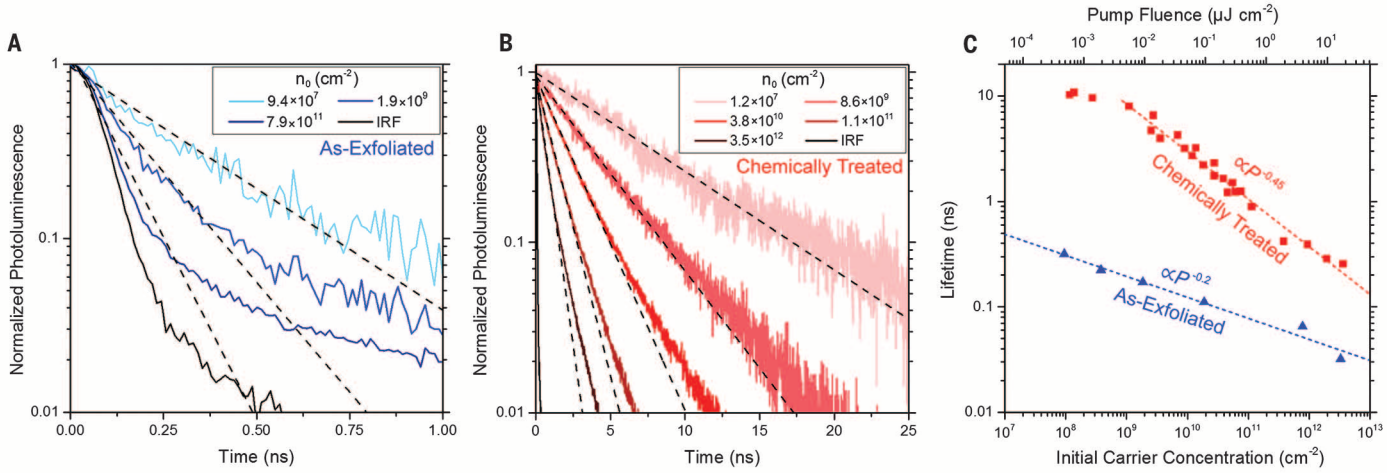

Fig. 3. Time-resolved luminescence. (**A**) Radiative decay of an as-exfoliated MoS_2 sample at various initial carrier concentrations (n_0), as well as the instrument response function (IRF). (**B**) Radiative decay of a treated MoS_2 sample plotted for several initial carrier concentrations (n_0), as well as the IRF. Dashed lines in (A) and (B) indicate single exponential fits. (**C**) Effective PL lifetime as a function of pump fluence. Dashed lines show a power law fit for the dominant recombination regimes.

undergo radiative recombination or nonradiatively recombine with a second exciton according to $B_r n^2 = \tau_r^{-1}\langle N\rangle + C_{bx}\langle N\rangle^2$ (*19*), where τ_r is the radiative lifetime and C_{bx} is the biexcitonic recombination rate. The QY is then given as

$$QY = \frac{\tau_r^{-1}\langle N\rangle}{\tau_r^{-1}\langle N\rangle + B_{nr}n^2 + C_{bx}\langle N\rangle^2} \quad (2)$$

For the case of the TFSI-treated sample, B_{nr} is negligible because the QY at low pump powers is >95%, allowing us to extract a biexcitonic recombination coefficient $C_{bx} = 2.8\ cm^2\ s^{-1}$. For the as-exfoliated sample, the defect-mediated nonradiative recombination can be fit to $B_{nr} = 1.5 \times 10^6\ cm^2\ s^{-1}$, using the same C_{bx} value. The fitting results are plotted as the dashed curves in Fig. 2B.

To investigate the carrier recombination dynamics, we performed time-resolved measurements on both as-exfoliated and chemically treated samples. The luminescence decay was nonexponential, but not in the standard form known for bimolecular (Bn^2) recombination (*17*). As-exfoliated monolayers of MoS_2 had extremely short lifetimes on the order of 100 ps (Fig. 3A and fig. S6) (*14*), consistent with previous reports (*21*). After treatment, we saw a substantial increase in the lifetime, which is shown at several pump fluences in Fig. 3A. Fitting was performed with a single exponential decay that described only the initial characteristic lifetime for a given pump intensity. After the pump pulse, the exciton population decayed, which resulted in nonexponential decay through reduced nonradiative biexcitonic recombination. At the lowest measurable pump fluences, we observed a luminescence lifetime of 10.8 ± 0.6 ns in the treated sample, compared with ~0.3 ns in the untreated case at a pump fluence of $5 \times 10^{-4}\ \mu J\ cm^{-2}$ (Fig. 3C). The contrast between panels A and B of Fig. 3 is consistent with the QY trend.

Urbach tails, which depict the sharpness of the band edges (*22*), were derived from the steady-state PL spectra via the van Roosbroeck–Shockley equation and are plotted in fig. S8. After treatment with TFSI, a noticeable decrease in the Urbach energy (E_0) from 17.4 to 13.3 meV was observed, indicating a reduction in the overall disorder from potential fluctuations and improved band-edge sharpness (*22*). A spatial map showing Urbach energy (fig. S8) (*14*) further indicates that the treatment was highly uniform. To evaluate stability, the QY in air for chemically treated MoS_2 was measured daily at a constant pump power over the course of 1 week, during which the sample was stored without any passivation in ambient lab conditions (20° to 22°C, 40 to 60% relative humidity), as shown in fig. S9 (*14*). The QY remained above 80% during this period, indicating that the treatment resulted in samples that were relatively stable.

We then turned our attention to the effect of TFSI treatment on other properties of MoS_2. The monolayer surface was imaged by atomic force microscopy (AFM) before and after treatment (Fig. 4A). No visible change to the surface morphology was observed. We also investigated the effect of the treatment on the electrical properties of a back-gated MoS_2 transistor. The transfer characteristics of this majority carrier device before and after treatment showed a shift in the threshold voltage toward zero, indicating that the native n-type doping in the MoS_2 was removed while the same drive current was maintained (Fig. 4B). An improvement in the subthreshold slope indicated that the treatment reduces interface trap states. The Raman spectra of an as-exfoliated and treated monolayer (Fig. 4C) showed that there was no change in the relative intensity or peak position. Thus, the structure of MoS_2 was not altered during treatment, and the lattice was not subjected to any induced strain (*23*). Because absolute absorption was used in the calibration of QY, we performed careful absorption measurements using two different methods (*14*), both before and after treatment (Fig. 4D). At the pump wavelength (514.5 nm), no measurable change of the absolute absorption from the treatment was observed. The strong resonances at 1.88 and 2.04 eV (corresponding to the A and B excitons, respectively) are consistent with previous reports (*12*). We then performed surface-sensitive x-ray photoelectron spectroscopy (XPS) on bulk MoS_2 from the same crystal used for micromechanical exfoliation. The Mo 3d and S 2p core levels (Fig. 4E) showed no observable change in oxidation state and bonding after treatment (*24*). Thus, an array of different techniques for materials characterization shows that the structure of the MoS_2 remains intact after TFSI treatment, with only the minority carrier properties (i.e., QY and lifetime) enhanced.

The effect of treatment by a wide variety of molecules is shown in table S1 and discussed in the supplementary text. Various polar, nonpolar, and fluorinated molecules, including strong acids and the solvents used for TFSI treatment (dichlorobenzene and dichloroethane), were explored. Treatment with the phenylated derivative of superacid TFSI was also performed (fig. S11) (*14*). These treatments all led to no or minimal (less than one order of magnitude) enhancement in PL QY.

The exact mechanism by which the TFSI passivates surface defects is not fully understood. Exfoliated MoS_2 surfaces contain regions with a large number of defect sites in the form of sulfur vacancies, adatoms on the surface, and numerous impurities (*25*–*27*). In fig. S12A (*14*), the calculated midgap energy is shown for several defect types, including a sulfur vacancy, adsorbed –OH, and adsorbed water. Deep-level traps—which contribute to defect-mediated nonradiative recombination, resulting in a low QY (*27*)—are observed for all of these cases. The strong protonating nature of the superacid can remove absorbed water, hydroxyl groups, oxygen, and other contaminants on the surface. Although these reactions will not remove the contribution of defects to nonradiative recombination, they will open the active defect sites to passivation by a second mechanism. One possibility is the protonation of the three dangling bonds at each sulfur vacancy site. However, density

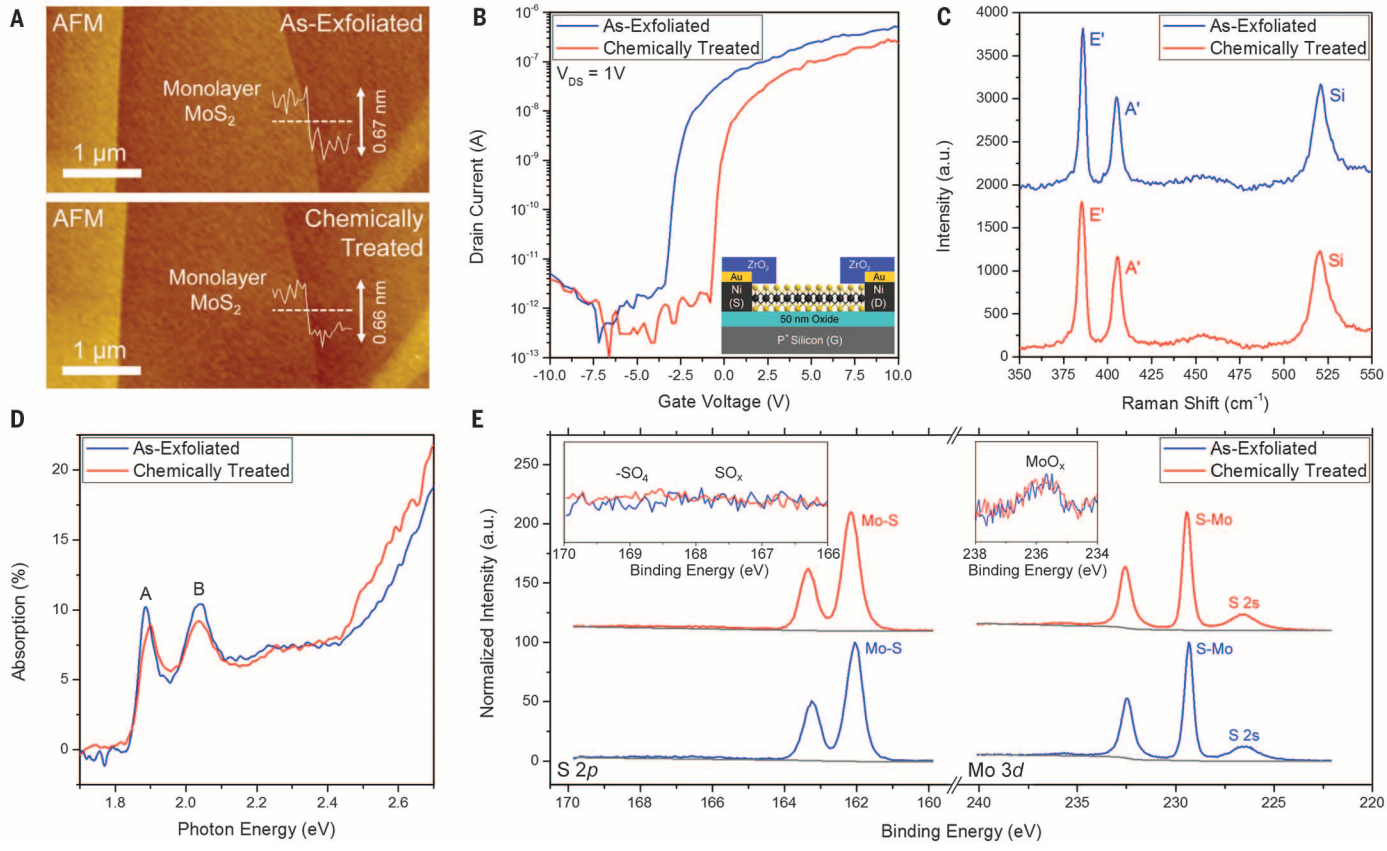

Fig. 4. Material and device characterization. (**A**) AFM images taken before and after TFSI treatment. (**B**) Transfer characteristics of a monolayer MoS_2 transistor, both before and after treatment. V_{DS}, drain-source voltage; S, source; D, drain; G, gate. (**C**) Raman spectrum of as-exfoliated and TFSI-treated MoS_2 samples. a.u., arbitrary units; E′, MoS_2 in-plane mode; A′, MoS_2 out-of-plane mode; Si, silicon Raman peak. (**D**) Absorption spectrum of the as-exfoliated and treated MoS_2 samples. A and B indicate the exciton resonances. (**E**) XPS spectrum of the S 2p and Mo 3d core levels before and after treatment. The insets show that there is no appearance of SO_x or change in the MoO_x peak intensity after treatment.

functional theory calculations (fig. S12C) (*14*) show that this reaction is energetically unfavorable. A second possibility is that the surface is restructured to reduce the sulfur vacancies through rearrangement of sulfur adatoms on the surface, which can be facilitated by hydrogenation via TFSI (*14*). The presence of sulfur adatom clusters has previously been confirmed by scanning tunneling microscopy and energy-dispersive x-ray spectroscopy (*27*–*30*). Careful examination of the XPS data over multiple spots before and after TFSI treatment (fig. S13) (*14*) reveals that the ratio of bonded sulfur to molybdenum (S/Mo) increased from 1.84 ± 0.04 in the as-exfoliated case to 1.95 ± 0.05 after treatment (table S2) (*14*).

We have demonstrated an air-stable process by which the PL of monolayer MoS_2 can be increased by more than two orders of magnitude, resulting in near-unity luminescence yield. This result sheds light on the importance of defects in limiting the performance of 2D systems and presents a practical route to eliminate their effect on optoelectronic properties. The existence of monolayers with near-ideal optoelectronic properties should enable the development of new high-performance light-emitting diodes, lasers, and solar cells. These devices can fulfill the revolutionary potential of the 2D semiconductors (*1*), which require interfacial passivation, as in all classic semiconductors.

REFERENCES AND NOTES

1. F. Xia, H. Wang, D. Xiao, M. Dubey, A. Ramasubramaniam, *Nat. Photonics* **8**, 899–907 (2014).
2. S. Wu *et al.*, *Nature* **520**, 69–72 (2015).
3. H. Fang *et al.*, *Proc. Natl. Acad. Sci. U.S.A.* **111**, 6198–6202 (2014).
4. L. Britnell *et al.*, *Science* **340**, 1311–1314 (2013).
5. K. F. Mak, K. He, J. Shan, T. F. Heinz, *Nat. Nanotechnol.* **7**, 494–498 (2012).
6. S. B. Desai *et al.*, *Nano Lett.* **14**, 4592–4597 (2014).
7. S. Tongay *et al.*, *Sci. Rep.* **3**, 2657 (2013).
8. A. Chernikov *et al.*, *Phys. Rev. Lett.* **113**, 076802 (2014).
9. H. M. Hill *et al.*, *Nano Lett.* **15**, 2992–2997 (2015).
10. T. C. Berkelbach, M. S. Hybertsen, D. R. Reichman, *Phys. Rev. B* **88**, 045318 (2013).
11. L. Yuan, L. Huang, *Nanoscale* **7**, 7402–7408 (2015).
12. K. F. Mak, C. Lee, J. Hone, J. Shan, T. F. Heinz, *Phys. Rev. Lett.* **105**, 136805 (2010).
13. H. Wang, C. Zhang, F. Rana, *Nano Lett.* **15**, 339–345 (2015).
14. Materials and methods are available as supplementary materials on *Science* Online.
15. I. Schnitzer, E. Yablonovitch, C. Caneau, T. J. Gmitter, *Appl. Phys. Lett.* **62**, 131–133 (1993).
16. Y. S. Park *et al.*, *Phys. Rev. Lett.* **106**, 187401 (2011).
17. P. T. Landsberg, *Phys. Status Solidi* **41**, 457–489 (1970).
18. F. Wang, Y. Wu, M. S. Hybertsen, T. F. Heinz, *Phys. Rev. B* **73**, 245424 (2006).
19. H. Wang *et al.*, *Phys. Rev. B* **91**, 165411 (2015).
20. C. Mai *et al.*, *Nano Lett.* **14**, 202–206 (2014).
21. T. Korn, S. Heydrich, M. Hirmer, J. Schmutzler, C. Schuller, *Appl. Phys. Lett.* **99**, 102109 (2011).
22. A. Iribarren, R. Castro-Rodriguez, V. Sosa, J. L. Pena, *Phys. Rev. B* **58**, 1907–1911 (1998).
23. Z. Liu *et al.*, *Nat. Commun.* **5**, 5246 (2014).
24. A. Azcatl *et al.*, *Appl. Phys. Lett.* **104**, 111601 (2014).
25. C. P. Lu, G. Li, J. Mao, L. M. Wang, E. Y. Andrei, *Nano Lett.* **14**, 4628–4633 (2014).
26. S. McDonnell, R. Addou, C. Buie, R. M. Wallace, C. L. Hinkle, *ACS Nano* **8**, 2880–2888 (2014).
27. R. Addou *et al.*, *ACS Nano* **9**, 9124–9133 (2015).
28. R. Addou, L. Colombo, R. M. Wallace, *Appl. Mat. Interfaces.* **7**, 11921–11929 (2015).
29. J. Y. Noh, H. Kim, Y. S. Kim, *Phys. Rev. B* **89**, 205417 (2014).
30. A. P. Nayak *et al.*, *Nat. Commun.* **5**, 3731 (2014).

ACKNOWLEDGMENTS

We thank F. R. Fischer for in-depth discussions on surface chemistry and A. B. Sachid for analysis of the electrical measurements. M.A., J.X., J.W.A., X.Z., and A.J. were funded by the Director, Office of Science, Office of Basic Energy Sciences, Materials Sciences and Engineering Division of the U.S. Department of Energy, under contract no. DE-AC02-05Ch11231. A.A., J.N., R.A., S.KC, R.M.W., and K.C. were funded by the Center for Low Energy System Technology (LEAST), one of six centers supported by the STARnet phase of the Focus Research Program (FCRP), a Semiconductor Research Corporation program sponsored by Microelectronics Advanced Research Corporation and Defense Advanced Research Projects Agency. D.K. acknowledges support from Samsung. E.Y. acknowledges support from the NSF Center for Energy Efficient Electronics Science (E^3S). J.-H.H. acknowledges support from the baseline fund of KAUST, and M.D. acknowledges support from the U.S. Army Research Lab Director's Strategic Initiative program on interfaces in stacked 2D atomic layers and materials.

SUPPLEMENTARY MATERIALS

www.sciencemag.org/content/350/6264/1065/suppl/DC1
Materials and Methods
Supplementary Text
Figs. S1 to S13
Tables S1 and S2
References (*31*–*48*)

12 August 2015; accepted 13 October 2015
10.1126/science.aad2114

Near-unity photoluminescence quantum yield in MoS_2

Matin Amani *et al.*

Science **350**, 1065 (2015);
DOI: 10.1126/science.aad2114